

Structure of the surface region of stainless steel: bulk and thin films

Debi Garai^{1,2,3}, Axel Wilson¹, Ilaria Carlomagno⁴, Carlo Meneghini⁴, Francesco Carla¹, Hadeel Hussain¹, Ajay Gupta², Jörg Zegenhagen^{1,*}

¹ Diamond Light Source Ltd, Harwell Science and Innovation Campus, Didcot, Oxfordshire, OX11 0DE, United Kingdom

² Amity Centre for Spintronic Materials, Amity University, Noida 201313, Uttar Pradesh, India

³ Amity Institute of Applied Sciences, Amity University, Noida 201313, Uttar Pradesh, India

⁴ Dipartimento di Scienze, Universita Roma Tre, Via della Vasca Navale 84, 00146 Rome, Italy

E-mail: jorg.zegenhagen@gmail.com

Abstract

The surface region of austenitic stainless steel (SS) is investigated by synchrotron X-ray powder diffraction (XRPD) and X-ray absorption near edge structure (XANES) measurements, because its composition and structure is crucial for the corrosion resistance of SS. Grazing incidence XRPD of a polished AISI 304 bulk steel sample show that the near-surface structure is modified. The concentration of the ferrite phase of Fe, a typical minority phase in AISI 304, increases gradually from 10% to 30% when approaching the surface from 150 nm depth. XANES Fe K-edge investigations of ultra-thin, sputter deposited films also reveal much larger ferrite fractions than expected from the austenitic steel composition of the films. Reasons for the increased ferrite fraction in the surface region of bulk steel and thin films are discussed. However, right at the surface, the trend reverses. Analysis of XANES data for an ultra-thin, 4 nm SS film show that 80% of Fe is oxidized and 20% of metallic Fe is present only in austenite structure, suggesting that ferritic iron is preferentially subject to oxidation. The austenitic Fe is located at more than 2 - 3 nm below the surface where the Ni concentration is > 10%.

Keywords

Stainless steel, surface structure, thin films, X-ray near edge structure, grazing incidence X-ray powder diffraction, synchrotron radiation

This article has been accepted for publication and undergone full peer review but has not been through the copyediting, typesetting, pagination and proofreading process, which may lead to differences between this version and the [Version of Record](#). Please cite this article as [doi: 10.1002/pssb.202100513](https://doi.org/10.1002/pssb.202100513).

1 Introduction

The present study reports about the austenite/ferrite composition in the very surface ($< \mu\text{m}$ depth) region of stainless steel (SS). The polycrystalline bulk structure of SS is dominated by the austenitic phase. The Ni-stabilized face centred cubic (fcc) structure provides superior corrosion resistance. At Ni concentration of around 10 %, the body centred cubic (bcc) ferrite phase, the typical structure of bulk iron, is in the minority in SS. However, by increasing the amount of ferrite in steel some mechanical properties such as strength and toughness can be improved. Of current use are here duplex (stainless) steels that contains ferrite and austenite roughly to equal amounts.

The current study is motivated by the fact that it is meanwhile well known that not only the global amount of austenite and ferrite in steel matters but their detailed distribution as well. Beyond mechanical performance, the local austenite/ferrite distribution, in particular close to the surface, also influences, affects or determines the corrosion resistance of steel [1 - 3]. It is important to realize in this context that the corrosion behaviour of (stainless) steel is ultimately determined by structure and composition of just the outer few nm of the surface [4]. However, reports about the austenite/ferrite composition of steel in the very near surface region ($< \mu\text{m}$ depth) appear to be scarce. Methods typically used for analysing the austenite/ferrite composition of steel are diffraction techniques without surface specificity, optical methods that are inherently exclusively sensitive to the outer surface texture or magnetic measurements that provide global bulk information [5].

Steel is a rather common material in our daily life and a backbone of modern civilization. Global crude steel production reached 1,875.0 million tonnes (Mt) in the year 2019 with China alone accounting for one billion tonnes [6]. The world-wide steel use per capita, in terms of finished steel products, was 216.3 kg in 2017 [7]. Because of its enormous importance, steel is still subject of intense ongoing research.

Steel components make up most of an automobile's mass. With the drive toward green technologies, there is presently a major push toward reducing the weight of steel components to increase fuel efficiency in order to reduce CO_2 emissions [8]. Thus, intense research focusses on making steel more formable, yet stronger and lighter to fulfil the same structural functions. Jeopardizing the strength and integrity of the material, corrosion has always been a major issue. For instance, recently, in the use of biodiesel as a new green energy source, corrosion of biodiesel-filled fuel tanks has become a major problem [9, 10].

Steel is heavily used in marine applications for ships, bridges, on-shore and off-shore structure [11] and it is extensively used in construction industries. Over one-quarter of steel produced annually is used in the construction of buildings [12].

Stainless steel is used for a wide range of medical applications, because of the ease of manufacturing, low cost, corrosion resistance, ease of cleaning and wide availability [13]. It is one of the most important materials for orthopedic implants. Different stainless steel alloys have been developed for medical use but the most frequently used medical grade stainless steel is the alloy AISI 316L [14].

There is hardly a niche in our daily life where we do not come into contact with steel products. If we measure the impact of all sorts of materials in use in our life at 100%, the impact of steel is largest, rated at 32% [15]. It is estimated that generally one quarter of the global energy consumption is used for the production of materials [15] and more efficient use of materials is nowadays becoming more and more important in order to reduce greenhouse gas emissions. This clearly calls for recycling of materials and avoiding wasteful loss. In this respect it is important to realize that major amounts of steel are simply destroyed and lost due to corrosion, making it subject of intense research.

Like all metals, especially alloys, steel is subject of galvanic corrosion in aqueous environments. When two dissimilar metals in electrical contact with each other are exposed to an electrolyte, a galvanic current flows from the one to the other and corrosion takes place on the anode of the couple [16]. On our water-rich planet, aqueous electrolytic corrosion is omnipresent and especially destructive for alloys like steel, where different metallic and non-metallic elements are in contact with each other on the microscopic scale. So-called stainless steels (SS) offer some corrosion resistance owing to a specific alloy composition, notably by a sufficiently high chromium concentration. With a chromium content of 18 to 20%, AISI 304 [17] and AISI 316 are among the most widely used stainless steels, where the composition of the latter differs from the former only by the addition of 2 to 3% of Mo.

The dominant (poly-)crystalline phase of AISI 300 series of steels is the face centered cubic (fcc) austenite γ -phase. Iron itself crystallizes at room temperature in the α -ferrite body centered cubic (bcc) structure and the stabilization of the austenite fcc phase in AISI 304/316 steel requires the addition of Ni, which adopts the fcc structure in its bulk form. A concentration of 8 to 12% is characteristic for the austenitic steels AISI 304 and AISI 316 [17]. However, austenitic steels such as AISI 304/316 can also contain a certain amount of body centered cubic (bcc) ferrite α/δ -phase depending on production and processing [18, 19].

Corrosion resistance of stainless steel is achieved by an ultrathin metal-oxide film of merely $\approx 2 - 3$ nm thickness, acting as a barrier. This passive layer prevents galvanic corrosion by hindering electrical transport and material diffusion from and to the underlying bulk of steel [20-4]. However, the protection is not perfect under all conditions. Reasons for the breakdown of the ultra-thin protective film and the microscopic processes involved at the onset of corrosion are subject of intense research [22]. Owing to its minute thickness, understanding of the cause of the onset of galvanic corrosion and following the atomistic mechanisms of the destruction of the metal-oxide film *in situ* are not easy tasks. It requires following processes in the surface with sub-monolayer sensitivity, despite the material being covered by electrolyte.

Very recently, we reported a novel approach to investigate early surface processes during galvanic corrosion of stainless steel by employing ultra-thin films and synchrotron X-radiation [23]. Using ultra-thin, 4 – 80 nm thick films for corrosion studies allows tracing *in situ*, with sub-monolayer sensitivity, under the presence of a bulk-like electrolyte layer, the material budget in the passive film during galvanic corrosion, employing X-ray spectroscopy and using the penetration power of X-rays. With 4 nm thick steel films, here denoted as 4 nm SS 304, exposed to 0.1 M KCl in an electrochemical cell, we monitored the onset of corrosion *in situ*, studying the breakdown of the passive layer in contact with the electrolyte as a function of applied steel-electrode potential on the atomic scale [23]. The films had been deposited on silicon substrates, SiN membranes and Ru/B4C multilayer (ML) by sputter deposition using AISI 304L and AISI 316 stainless steel as target material. AISI 304 and AISI 316 are very similar, except that AISI 316 exhibits higher pitting corrosion [24] resistance due to the addition of 2 to 3% of Mo [17]. The 304L variant has a slightly lower carbon content (0.03%) instead of 0.08% for AISI 304 [17].

An important part of the investigation involved the characterisation of the thin films using X-ray diffraction and spectroscopy, which proved that they represent excellent replicas of the (near-)surface region of steel in terms of structure, chemistry and composition. The results of X-ray absorption near edge structure (XANES) [25] measurements, obtained for an about 4 nm SS 304 film have been published recently [23, 26] and are reproduced in Fig. 1. Analysis of the chemical sensitive XANES spectra revealed quantitatively the degree of oxidation of the three main metallic elements, i.e. iron, chromium and Nickel. The fit to the data using the ATHENA [27] software revealed (with an error of $\pm 5\%$) that 84%, 67% and 20% of chromium, iron and nickel, respectively are oxidized. Combining XANES measurements with the XSW technique [28 - 31] allowed to probe the metal-oxidation states in the film depth selectively [32]. The results revealed that the metal oxidation is limited to the outer 2 – 3 nm surface region of the SS 304 film [23, 26].

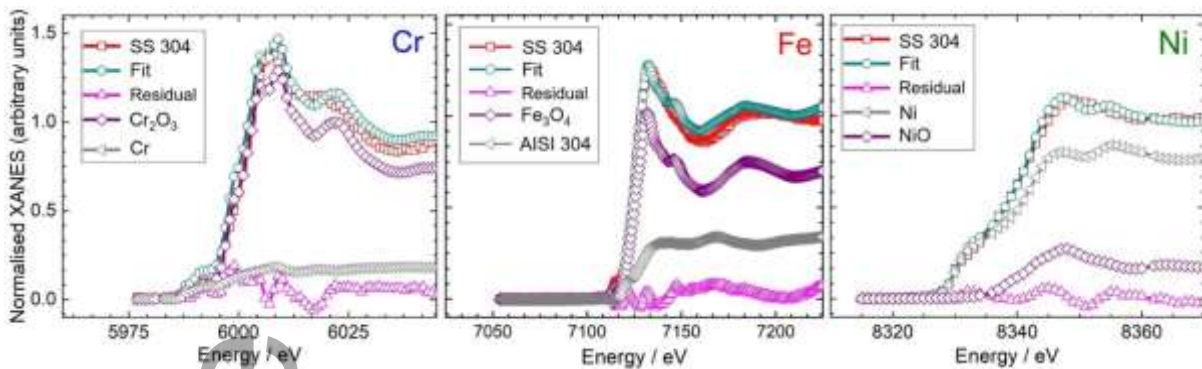


Figure 1 XANES data of 4 nm SS 304 film at the Cr, Fe and Ni edge. Fit to the data using corresponding reference spectra revealed (with an error of $\pm 5\%$) the degree of metal oxidation : 84%, 67% and 20% of chromium, iron and nickel, respectively are oxidized. (Taken from [24])

The depth distribution of Fe, Cr, and Ni, the three main elements of a 4 nm SS 304 steel in the film, was also analysed with the help of X-ray standing wave (XSW) measurements. The XSW analysis of the 4 nm SS 304 film on a Ru/B₄C multilayer has been published recently [26, 23]. The results, reproduced in Fig. 2, reveal strong segregation in the surface region with (oxidized) Fe exclusively covering ≈ 0.5 nm of the surface. Chromium, mostly oxidized, is found below, whereas Ni, mostly metallic, is hidden at a depth exceeding ≈ 2 nm.

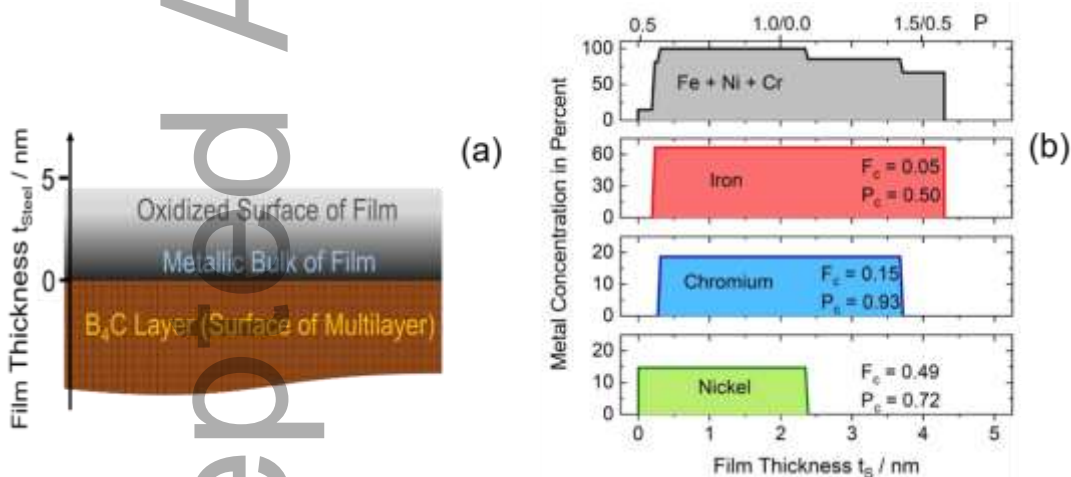


Figure 2 Results of the XSW analysis of the metal distribution in the 4 nm SS 304 film on the RuB₄C multilayer. (a) Schematic representation. (b) Results of the XSW analysis [26].

These findings for the thin films are in accordance with earlier reports of the structure of bulk steel samples [33 - 35]. This is interesting on its own since it suggests that the main reason for the metal segregation and the specific layering is the minimization of the surface energy, suggesting that Fe-oxide has a lower surface energy than Cr-oxide in turn lower than for nickel(-oxide).

In the present publication we investigate the (near-) surface structure of steel further and reveal that even the crystalline structural composition of steel is modified, however reaching (much) further, $\approx \mu\text{m}$ deep into the bulk. Using grazing incidence powder X-ray diffraction (GIXRD) and a polished AISI 304 bulk steel sample, we show that the bcc ferrite structure becomes gradually more prominent when approaching the surface from a depth of > 150 nm. A much higher ferrite fraction than expected from their austenitic steel composition is also observed for thin films. Only in an ultra-thin film of ≈ 4 nm, the metallic Fe phase is austenitic and no bcc ferrite could be identified by XANES, which suggests that (exclusively) the bcc iron in the surface region has been oxidized.

2 Experimental

The structural analysis of the steel surface region was carried out using synchrotron radiation at two state of the art beamlines. Grazing incidence X-ray powder diffraction (GIXRPD) measurements were performed at the I07 surface diffraction beamline [36] at Diamond Light Source Ltd. at Rutherford Appleton lab, Didcot, UK, using mirror focussed X-rays set at 9.2 keV and the six circle kappa diffractometer with a 2D pixel detector (Pilatus 100 k from Dectris). As sample served a 2 mm thick, annealed (as specified by the supplier) austenitic stainless steel platelet (AISI 304 from Goodfellows), polished to optical finish by surface preparation laboratory in Netherlands. AISI 304 contains 18 to 20 % chromium, 8 to 12 % nickel, about 3% other elements such as manganese, silicon, carbon, etc., with the remainder being iron. Depth resolved structural information was obtained by varying the angle of incidence of the X-rays. Corresponding attenuation lengths are estimated/calculated using the center of X-ray optics (CXRO) data server at Lawrence Berkeley Lab [37] and an average steel metal composition with 10%, 20% and 70% of Ni, Cr and Fe.

X-ray absorption near edge structure (XANES) measurements at the Fe K-edge around 7112 eV were carried out at the absorption spectroscopy beamline P64 at the PETRA III storage ring at DESY, Hamburg, Germany [38]. The investigated stainless steel thin films were produced by sputter deposition from AISI 304L targets, as described in detail in a recent publication [23]. AISI 304L steel consists to 97% of Fe, Cr and Ni. The concentrations of these three metals in the thin films, as determined by quantitative X-ray fluorescence analysis [23], were found to be in the range typical for austenitic 304 steel. . The steel thin films are denoted as SS 304 in the following. The films were deposited with the substrate held at room temperature without any post-deposition treatment. They were kept for weeks under normal ambient conditions before the investigations. Employing a multi-element solid state detector [38], emission mode XANES measurements of the thin films were carried out at grazing angle of incidence to enhance the surface sensitivity and suppress fluorescence from the substrates. The XANES spectra of the thin films were analysed by fitting linear combinations of Fe XANES spectra of bulk iron, AISI 304 steel and Fe-oxides to the data using the ATHENA program [27].

A 5 μm thick foil of AISI 304 steel, also obtained from Goodfellows, was used to record a XANES reference spectrum for Fe in austenitic steel. The corresponding measurements were performed in transmission geometry, thus avoiding surface effects. Simplifying, for the purpose of reference, this XANES spectrum is assumed in the following to be typical for Fe being present to 100% in austenitic environment, i.e. in the fcc structure. Other Fe XANES spectra needed for fitting the thin film data namely of bulk iron, i.e. Fe with bcc structure, and Fe-oxides had been obtained from elsewhere [39].

3 Results

3.1 X-ray powder diffraction

The results of GIXRPD measurements of a polished AISI 304 sample are shown as a function of grazing angle in Fig. 3 with the austenite fcc peak at about 37.6 degree and ferrite bcc peak at about 38.3 degree. The corresponding attenuation lengths for the different angles of incidence, i.e. the penetration depths of the incident X-rays, are shown as a function of the angle of incidence in the right hand part of Fig. 3. Decreasing the angle from 1.5 to 0.2 degree, the mean X-ray penetration depth decreases from 150 to 2 nm.

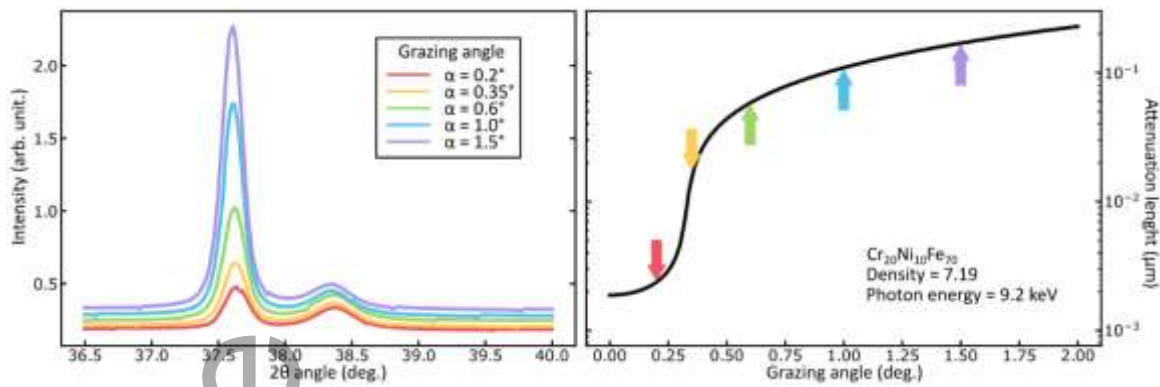


Figure 3 Left hand: X-ray powder diffraction data as a function of incidence angle with fcc peak at about 37.6 degree and bcc peak at about 38.3 degree. Right hand: penetration depth as a function of angle of incidence with the five angles used on the left marked in the figure.

From the shallowest angle incidence (0.2 degree) to the highest angle of incidence (1.5 degree) the penetration depth increases from 2 nm to 150 nm and the austenite to ferrite peak intensity ratio a/f changes from roughly $a/f = 2$ to $a/f = 10$. This means that closer to the surface roughly 30% of the steel adopts the ferrite structure compared to only about 10% in the bulk. From the width of the diffraction peaks the fcc and bcc grain sizes can be estimated being about 40 nm and 30 nm, respectively.

Recently, $\theta - 2\theta$ powder XRD (XRPD) data were published (reference [23], fig. 2) of the AISI 340 steel that had been used as target for the sputter deposition of the thin films used in the present study as well as XRPD of another ≈ 100 nm thick film that had been produced by 15 minutes sputter deposition (Fig. 3 in reference [23]). Those measurements had been carried out using a Cu $K\alpha$ lab source (X-ray energy of 8.04 keV). With an angle of incidence of roughly 22 degrees for the fcc (111) and bcc (110) peak, the mean probing depth of the X-rays can be calculated to $\approx 1.5 \mu\text{m}$, significantly larger than for the GIXRPD measurements shown in Fig. 3. For the bulk target-steel, the ratio of the integral intensities of the fcc (111) to bcc (110) peak a/f was determined to about 4, i.e. significantly smaller than for the polished AISI 304 sample with $a/f = 10$ for the largest grazing angle (largest mean penetration depth). Thus, about 20% of Fe in the target steel were found adopting the ferrite structure compared to only 10% in the polished steel sample at penetration depths of 1.5 and 0.15 μm , respectively. For the $\approx 0.1 \mu\text{m}$ thin film with $a/f = 2$ the corresponding ratio was found even smaller, meaning that about 30% of the Fe in this thin film was found in bcc environment.

However, as reported in reference [23], the fit of the data of the ≈ 100 nm film visibly did not reproduce the austenite (111) and ferrite (110) peak shapes very well. This can be understood, since with decreasing film thickness and thus increasing film shape-anisotropy, crystalline grains in the thin films will unavoidably become smaller on average and the size distribution will become inhomogeneous and anisotropic. The less well pronounced X-ray peak profiles of the thin film in figure 3 of reference [23] indicate indeed a more inhomogeneous size distribution in comparison with the bulk steel. Decreasing and inhomogeneous grain size are associated with diffraction peak broadening and peaks eventually vanish in the background (peak broadening will reach 2 degree for 4 nm grains) and the diffraction data become unreliable. Furthermore, for thin films, (surface) oxidation must be taken into account. Determining the austenite/ferrite ration by fitting the austenite and ferrite XRD peaks for thin films thus becomes unreliable. Because of this, we relied on XANES analysis for determining the austenite and ferrite (and oxide) composition in the thin films.

3.2 XANES analysis of SS 304 thin films

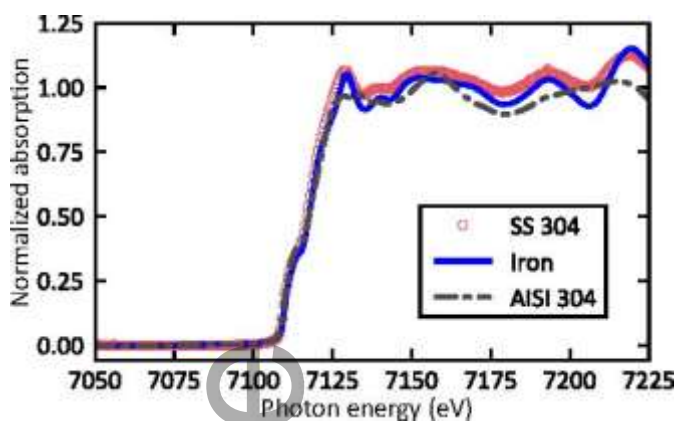


Figure 4 XANES spectra of Fe, AISI 304 steel and an 80 nm thick SS 304 film, all roughly scaled to the same intensity.

For determination of the Fe environment in the films we relied on fitting Fe XANES spectra using linear combination fits (LCFs) employing as reference Fe XANES spectra of materials with Fe in different environments.

Figure 4 shows for comparison normalized XANES spectra taken at the Fe K-edge for Fe in bulk iron, AISI 304 steel and an 80 nm SS 304 film. The three spectra clearly differ, in particular for Fe in bulk iron (bcc) and steel (fcc) environment. Figure 5 shows a linear combination fit (LCF) to the SS 304 80 nm film XANES data using the ATHENA program and Fe spectra from AISI 304 steel, bulk iron and FeO samples. It reveals that in the 80 nm film ($63 \pm 5\%$) Fe are in the bcc and only ($28 \pm 5\%$) Fe is in the fcc austenite structure with the remainder ($9 \pm 5\%$) of the Fe being oxidised. The fit results show more bcc than fcc Fe (twice as much) in the 80 nm film, i.e. $a/f = 0.5$. This may be compared with the XRPD results of the thicker, 100 nm film (cf. Fig. 3, reference [23]) that gave $a/f = 2$, i.e. twice as much austenite (fcc) as ferrite (bcc). Already at this point it is important to stress the complementarity of XANES and XRD. While XRD is (only) probing the long range coherent phase, XANES is sensitive to the local atomic structure [25].

The metal composition in the films had been determined by quantitative X-ray fluorescence analysis [23]. In terms of Fe/Ni, Fe/Cr and Cr/Ni concentration ratios, for the 80 nm (4 nm) SS 304 film the measurements had revealed values of 9.2 (9.0), 4.3 (4.3) and 2.1 (2.1), respectively. Since in AISI 304 Fe, Cr and Ni together represent roughly 97% of the total material [17], the measured ratios translate to Ni and Cr concentrations c_{Ni} and c_{Cr} , respectively in the 80 nm (4 nm) film of $c_{Ni} = 8\%$ and $c_{Cr} = 17\%$. In austenitic AISI 304 steel, Ni and Cr concentrations should be ranging from $8\% \leq c_{Ni} \leq 12\%$ and $18\% \leq c_{Cr} \leq 20\%$ [17]. Thus, the Cr and Ni concentration in 80 nm (4 nm) film are at the lower limit for austenitic steel.

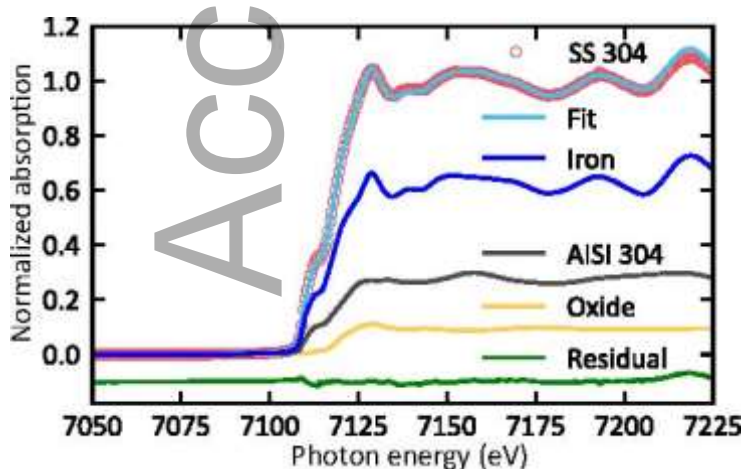


Figure 5 Fe XANES data of a 80 nm SS 304 and a LCF using the ATHENA program and Fe XANES data of bulk AISI 304, iron and oxide. The fit reveals that ($63 \pm 5\%$), ($28 \pm 5\%$), and ($9 \pm 5\%$) of the Fe is in the bulk-Fe (bcc), AISI (fcc) and oxide (FeO) phase, respectively.

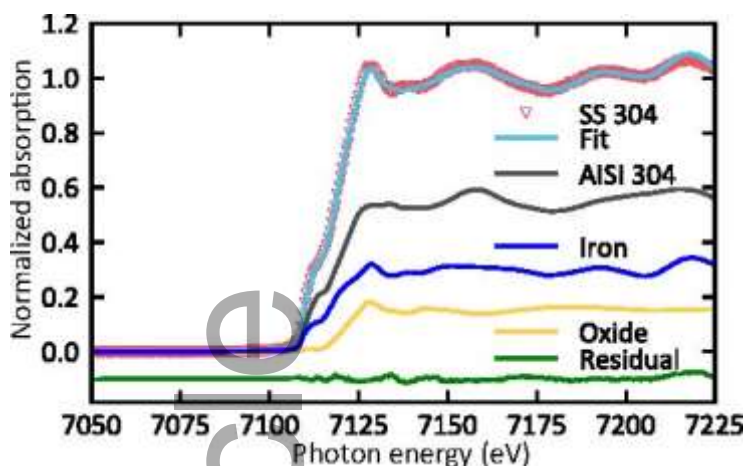


Figure 6 Fe XANES data for a 50 nm SS 304 film (data) and LCF using a combination of Fe XANES spectra of bulk AISI 304 steel, iron, and oxides ($\text{FeO} + \text{Fe}_3\text{O}_4$). The data are best fitted with $(60 \pm 5)\%$, $(30 \pm 5)\%$ and $(10 \pm 5)\%$ Fe in the fcc, bcc and oxide phase, respectively.

The results of Fe XANES measurement for a 50 nm SS 304 film are shown in Fig. 6. A fit to the data, using the ATHENA program and a linear combination of Fe XANES spectra from AISI 304 foil, bulk iron and from Fe-oxides, reveals that the Fe XANES spectrum of the 50 nm SS 304 film is best fitted with $(60 \pm 5)\%$, $(30 \pm 5)\%$ and $(10 \pm 5)\%$ Fe in the fcc, bcc and oxide phase, respectively. Here, FeO and Fe_3O_4 are contributing roughly to the same amount (5%). Thus the austenite to ferrite ratio a/f equals 2. Worthy of mention, for this film, compared to the 80 nm film, XRF had revealed higher Ni and Cr concentrations $c_{\text{Ni}} = 10\%$ and $c_{\text{Cr}} = 22\%$, respectively, compared to $c_{\text{Ni}} = 8\%$ and $c_{\text{Cr}} = 17\%$ for the 80 nm film.

The Fe XANES data for an ultra-thin, 4 nm thick sputter-deposited SS 304 film are shown in Fig. 7. The Fe spectrum from the SS 304 thin film is markedly smoother compared to those of the 50 nm and 80 nm films. This points out a larger local disorder around the Fe in the ultra-thin film. The Fe XANES spectrum from the SS 304 film is best reproduced using a linear combination of spectra of Fe_3O_4 and AISI 304 with a weight of $(79 \pm 5)\%$ and $(21 \pm 5)\%$. This means that within the limits of error (about $\pm 5\%$) there is no bcc structure found in the film. The metallic part of Fe in the film is exclusively present in the form of fcc austenite phase and four fifth of the film, i.e. ≈ 3 nm are oxidized.

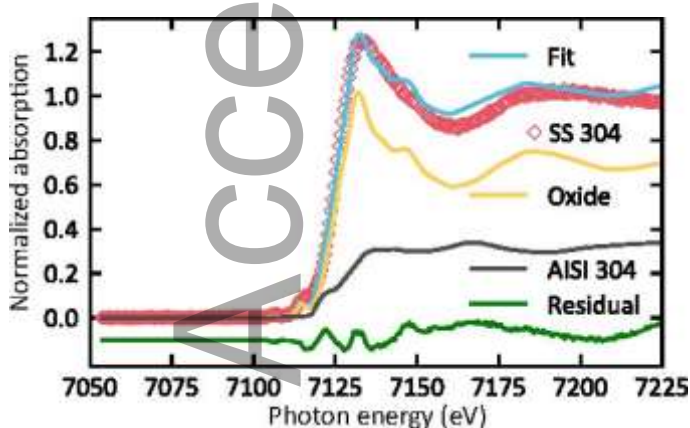


Figure 7 Fe XANES data for 4 nm SS 304 film and LCF with the help of the ATHENA program using Fe XANES spectra from AISI 304, bulk iron, and oxide. Best fit is obtained with $(79 \pm 5)\%$ Fe_3O_4 , $(21 \pm 5)\%$ AISI 304 and 0% bulk iron spectra.

4 Discussion and conclusion

The presented GIXRPD results (cf. Fig. 3) show clearly that the bcc (ferrite) to fcc (austenite) ratio in the surface region of stainless steel is not constant, but that the fraction of ferrite increases when approaching the surface. That austenitic stainless steel usually contains some amount of ferrite in the bulk is a well-known fact. In the bulk of AISI 304, probed by ferritscope on a macroscopic (mm) scale, the bcc delta ferrite fraction was found to vary between about 2% and 11%. [40].

It is also well known that the austenite to ferrite ratio depends sensitively on treatment [41] such as cooling rate [40]. For instance, when the austenite phase is quickly quenched to low temperature, a displacive, martensitic transformation leads to the formation of the bcc or body centered tetragonal (bct) structure [42]. Very important for the crystal structure of steel is the material composition. In particular, a sufficient concentration of Ni is required in order to stabilize the fcc structure of austenitic steel.

The presented results appear to show some discrepancies and even seemingly contradictory findings. Some discrepancies are already obvious for the two investigated bulk samples. Probing the polished AISI 304 sample by GIXRPD, analysis reveals that it contains more than 30% ferrite at the very surface, decreasing to about just 10% at the largest sampled depth of ≈ 150 nm. For an even larger probed depth of ≈ 1.5 μm , XRPD $\theta - 2\theta$ measurements of the (unpolished) AISI 304 steel sample, which was used as target for sputter deposition of the thin films, showed a larger ferrite fraction of about 20%. In view of the above said, we believe that this discrepancy can be explained sufficiently by different histories of treatment of these two samples. Even besides polishing, both AISI 304 specimen almost certainly underwent different production processes. Furthermore, differences in Ni concentration cannot be excluded either, which would also affect the amount of austenite and ferrite in the material.

Interestingly, the ferrite to austenite ratio is also significantly enhanced in the thin films, while their metal composition is proven to be compatible with austenitic stainless steel [23]. Thus, the thin films appear to be reflecting the behaviour of the investigated bulk steel surface region. This confirms our earlier conclusions that steel thin films represent valuable replicas of the surface region of stainless steel [26, 23] despite the fact that the “production” histories of the bulk steel samples and the thin films are obviously quite different. Analysis of the XANES data of the 50 nm film reveals that 30% of the iron is adopting the ferrite structure, which can be compared with the GIXRPD results on the polished steel sample. At 0.6 degree grazing angle, corresponding to an attenuation length of 52 nm, about 20% of iron is found in the ferrite structure, i.e. a very comparable amount. It is important to note that with 10%, the nickel concentration in the film was exactly what it should be for austenitic steel. The XRPD results for the thicker ≈ 100 nm film, reported in section 3.2, show also about 30% of Fe in the ferrite structure, similar to the results on the 50 nm film, despite its larger thickness. The analysis of the XANES data of the 80 nm film suggest that 60% of the iron have adopted the ferrite structure, but with $c_{\text{Ni}} = 8\%$ this film showed slightly reduced Ni concentration. Obviously, some variations of the ferrite concentration may be caused by variations in the nickel concentration.

However, when comparing the XANES and XRPD results, as mentioned above, it has to be taken into account that XANES and (GI)XRPD measurements provide (largely) complementary information. Whereas XANES measurements are exclusively sensitive to short-range (≈ 1 nm) order, XRPD measurements require some long-range (\gg nm) crystalline structure. In this context it is interesting to note that in the high resolution GIXRPD data (cf. Fig. 3) the bcc peak-width is noticeably (about 50 %) broader than the fcc peak-width, which means that the bcc crystallites in the polycrystalline steel are overall smaller than the fcc crystallites. Thus, it is reasonable to argue that some of the Fe in disordered bcc phase and smaller bcc nuclei may be missed at all by XRPD measurement whereas it will increase the XANES signal, by which reason XANES may show a larger bcc concentration than XRPD. Furthermore, it should be mentioned that annealing and mechanical deformation is known to introduce some weak texture in bulk steel samples [43, 44], which could also have influenced the results of the XRD measurements.

While the concentration of ferritic iron is found to increase when approaching the surface, the analysis of the XANES data for the thinnest film (≈ 4 nm) shows that it contains a major fraction of oxidized Fe having largely disordered (amorphous) local structure. The result of LCF is consistent with Fe in the Fe_3O_4 phase (79%) and a minority in the metallic austenite fcc phase (21%) while no Fe in the bcc ferrite phase is found. Thus, it seems to be safe to conclude that all bcc (and only bcc) iron in the surface region has been oxidized. Consulting Fig. 2b, it is obvious that the Fe in the austenitic phase of steel will be located at a depth below 2 - 3 nm where the Ni concentration is above 10%.

The presented GIXRPD results show clearly that the ferrite to austenite ratio in the surface region of stainless steel is not constant, but a function of depth. Reasons for this cannot conclusively be given based on the presented results but will require further investigation. Metal segregation and metal concentration gradients could play a role. In fact, the presented data seem to provide evidence that some increase of ferrite fraction may be the consequence of nickel poor environment. However, a relative high ferrite fraction of 30% is also found in a 50 nm film with sufficiently high Ni concentration - a ferrite concentration that is in reasonable agreement with the 20% ferrite concentration found in a probed depth of ≈ 50 nm in the polished bulk steel sample.

At any rate, similar findings for the investigated thin films and the bulk sample strongly suggest that the increase of the ferrite fraction is a surface/interface effect caused by whatever reason. It could be related to surface/interface strain that may reach μm deep into the bulk. In fact strain has been reported to be responsible for transforming austenite to ferrite in stainless steel [45]. The observed segregation and oxidation of the surface will certainly introduce large strain. Furthermore, strong surface/interface strain would also be caused by hydrogen diffusion. We recently reported that cathodic hydrogen loading is stressing the steel surface immensely [26]. However, with concentrations in the ppm range, it is questionable whether the hydrogen concentration in steel following hydrogen in-diffusion under ambient conditions [46, 47] could introduce sufficient strain.

In summary, the presented results provide further evidence of earlier conclusions [23] that sputter deposited steel films represent useful replicas of the (near) surface region of steel. The fraction of austenitic steel in the thin films is reduced compared to bulk steel. The presented GIXRPD results clearly demonstrate that this mimics the behaviour of bulk steel samples where the fraction of ferritic steel increases, when approaching to the surface, by at least 300% from about $\leq 10\%$ in the bulk to $\approx 30\%$. The XANES results on an ultra-thin 4 nm film reveal that Fe is oxidized to 80% and the remaining metallic Fe (20%) is left 2 -3 nm below the surface exclusively in the nickel-rich austenitic phase.

Acknowledgements

The research leading to this publication was supported by the project CALIPSOplus under the grant agreement 730872 from the EU Framework Programme for Research and Innovation HORIZON 2020. The experimental work was carried out at beamline P64 at DESY, a member of the Helmholtz Association (HGF) and I07 of Diamond Light Source Ltd. The authors would like to thank Wolfgang Caliebe and Vadim Murzin for help and advice during the experiments at P64. A.W. has received funding from the European Union's Horizon 2020 research and innovation program under the Marie Skłodowska-Curie grant agreement (GA) no 665593 awarded to the Science and Technology Facilities Council. D.G. acknowledges financial support by the by DST/INSPIRE Fellowship/[IF160579], awarded by the Government of India Ministry of Science and Technology.

References

- [1] P.K. De, N.R. Bandyopadhyay, D.K. Bhattacharya, *Mater. Charact* **2005**, *54*, 141, <https://doi.org/10.1016/j.matchar.2004.11.004>.
- [2] Cem Örnekk, Christofer Leygraf, Jinshan Pan, *Mater. Degrad.* **2019**, *3:8* ; <https://doi.org/10.1038/s41529-019-0071-8>.
- [3] S. Krishnan, J. Dumbre, S. Bhatt, E. Akinlabi, R. Ramalingam, *Int. J. Mech. Mechatron.* **2013**, *7(4)*, 650.
- [4] C.-O. A. Olsson, D. Landolt, *Electrochim. Acta* **2003**, *48*, 1093, [https://doi.org/10.1016/S0013-4686\(02\)00841-1](https://doi.org/10.1016/S0013-4686(02)00841-1).
- [5] A. Putz, M. Althuber, A. Zelić, E. M. Westin, T. Willidal, N. Enzinger, *Weld World* **2019**, *63*, 1075, <https://doi.org/10.1007/s40194-019-00721-4>.
- [6] See e.g. <https://www.worldsteel.org/>
- [7] Abhinav Bhaskar, Mohsen Assadi, Homam Nikpey Somehsaraei, *Energies* **2020**, *13*, 758, <https://doi.org/10.3390/en13030758>.
- [8] Miklos Tisza, Imre Czinege, *Int. J. Lightweight Mater. Manuf.* **2018**, *1*, 229, <https://doi.org/10.1016/j.ijlmm.2018.09.001>.
- [9] Deyab, M.A., Mohsen, *Sci. Rep.* **2021**, *11*, 16832 (2021). <https://doi.org/10.1038/s41598-021-96358-9>.
- [10] Savita Kaul, R.C. Saxena, Ajay Kumar, M.S. Negi, A.K. Bhatnagar, H.B. Goyal, A.K. Gupta, *Fuel Process. Technol.* **2007**, *88*, 303, <https://doi.org/10.1016/j.fuproc.2006.10.011>.
- [611] Srinivasan Chandrasekaran, Arvind Kumar Jain, *Materials for Ocean Structures*, chapter 3, in: *Ocean Structures*, CRC Press, 2016, <https://www.routledgehandbooks.com/doi/10.1201/9781315366692-4>.
- [12] Muiris C. Moynihan, Julian M. Allwood, *Proc. R. Soc. A* **2014**, *470*:20140170, <http://doi.org/10.1098/rspa.2014.0170>.
- [13] H. Ahirwar, Y. Zhou, C. Mahapatra, S. Ramakrishna, P. Kumar, H.S. Nanda, *Coatings* **2020**, *10*, 264, <https://doi.org/10.3390/coatings10030264>.
- [14] See e.g.: D.C. Tapscott, C. Wottowa, *Orthopedic Implant Materials*. [Updated 2021 Jul 31]. In: StatPearls [Internet]. Treasure Island (FL): StatPearls Publishing **2021** Jan-. Available from: <https://www.ncbi.nlm.nih.gov/books/NBK560505/#>
- [15] Edgar G. Hertwich *et al*, *Environ. Res. Lett.* **2019**, *14* 043004, <https://iopscience.iop.org/article/10.1088/1748-9326/ab0fe3>.
- [16] X. G. Zhang, *Uhlig's Corrosion Handbook*, Third Edition, (Ed: R. W. Revie), John Wiley & Sons, New York **2011**, pp. 123–143.
- [17] See e.g.: AK Steel Corporation **2018**, 304 / 304L Stainless Steel, <https://aksteel.com/sites/default/files/2018-11/304-304l-stainless.pdf>.
- [18] S. Venugopal, S.L. Mannan, Y.V.R.K. Prasad, *Mater. Lett.* **1996**, *26*, 161, [https://doi.org/10.1016/0167-577X\(95\)00215-4](https://doi.org/10.1016/0167-577X(95)00215-4)
- [19] P. Mayr, T.A. Palmer, J.W. Elmer, E.D. Specht, S.M. Allen, *Metall. Mater. Trans. A* **2010**, *41*, 2462, <https://doi.org/10.1007/s11661-010-0371-7>.

- [20] A. Kocijan, C. Donik, M. Jenko, *Corros. Sci.* **2007**, *49*, 2083, <https://doi.org/10.1016/j.corsci.2006.11.001>.
- [21] R. Jiang, Y. Wang, X. Wen, C. Chen, J. Zhao, *Appl. Surf. Sci.* **2017**, *412*, 214, <https://doi.org/10.1016/j.apsusc.2017.03.155>.
- [22] Vincent Maurice, Philippe Marcus, *Prog. Mater. Sci.* **2018**, *95*, 132, <https://doi.org/10.1016/j.pmatsci.2018.03.001>.
- [23] Debi Garai, Vladyslav Solokha, Axel Wilson, Ilaria Carlomagno, Ajay Gupta, Mukul Gupta, V Raghavendra Reddy, Carlo Meneghini, Francesco Carla, Christian Morawe, Jörg Zegenhagen, *J. Phys.: Condens. Matter* **2021**, *33*, 125001, <https://doi.org/10.1088/1361-648x/abd523>.
- [24] G. S. Frankel, *J. Electrochem. Soc.* **1998**, *145*, 2186, <https://doi.org/10.1149/1.1838615>.
- [25] A. Bianconi, *Appl. Surf.* **1980**, *6*, 392, [https://doi.org/10.1016/0378-5963\(80\)90024-0](https://doi.org/10.1016/0378-5963(80)90024-0).
- [26] Debi Garai, Ilaria Carlomagno, Vladyslav Solokha, Axel Wilson, Carlo Meneghini, Christian Morawe, Vadim Murzin, Ajay Gupta, Jörg Zegenhagen, *Phys. Status Solidi B* **2020**, *257*, 2000055, <https://onlinelibrary.wiley.com/doi/10.1002/pssb.202000055>.
- [27] B. Ravel, M. Newville, *J. Synchrotron Rad.* **2005**, *12*, 537, <https://doi.org/10.1107/S0909049505012719>.
- [28] B. W. Batterman, *Phys. Rev.* **1964**, *133*, A759, <https://doi.org/10.1103/PhysRev.133.A759>.
- [29] The X-Ray Standing Waves Technique: Principles And Applications (Eds: J. Zegenhagen, A. Y. Kazimirov), World Scientific, Singapore 2013.
- [30] J. Zegenhagen, *Jpn. J. Appl. Phys.* **2019**, *58*, 110502, <https://doi.org/10.7567/1347-4065/ab4dec>.
- [31] J. Zegenhagen, *Surf. Sci. Rep.* **1993**, *18*, 202, [https://doi.org/10.1016/0167-5729\(93\)90025-K](https://doi.org/10.1016/0167-5729(93)90025-K).
- [32] A. Gupta, D. Kumar, C. Meneghini, J. Zegenhagen, *J. Appl. Phys.* **2007**, *101*, 09D117, <https://doi.org/10.1063/1.2711698>.
- [33] C.L. Briant, R.A. Mulford, *Metall. Trans. A* **1982**, *13*, 745, <https://doi.org/10.1007/BF02642387>.
- [34] Y. Gui, Z.J. Zheng, Y. Gao, *Thin Solid Films* **2016**, *599*, 64, <https://doi.org/10.1016/j.tsf.2015.12.039>.
- [35] [17] L. Ma, F. Wiame, V. Maurice. P. Marcus, *NPJ Mater. Degrad.* **2019**, *3*, 29, <https://doi.org/10.1038/s41529-019-0091-4>.
- [36] C. Nicklin, T. Arnold, J. Rawle and A. Warne, *J. Synchrotron Rad.* **2016**, *23*, 1245, <https://doi.org/10.1107/S1600577516009875>.
- [37] https://henke.lbl.gov/optical_constants/
- [38] W.A. Caliebe, V. Murzin, A. Kalinko, M. Görlitz, *AIP Conf. Proc.* **2019**, *2054*, 060031, <https://doi.org/10.1063/1.5084662>.
- [39] Carlo Meneghini, private communication
- [40] Marcelo Aquino Martorano, Caio Fazzioli Tavares, Angelo Fernando Padilha, *ISIJ International* **2012**, *52*, 1054, <https://doi.org/10.2355/isijinternational.52.1054>.
- [41] S. Venugopal, S.L. Mannan, Y.V.R.K. Prasad, *Materials Letters* **1996**, *26*, 161, [https://doi.org/10.1016/0167-577X\(95\)00215-4](https://doi.org/10.1016/0167-577X(95)00215-4).

- [42] Hiromoto Kitahara, Rintaro Ueji, Nobuhiro Tsuji, Yoritoshi Minamino, *Acta Materialia* **2006**, *54*, 1279, <https://doi.org/10.1016/j.actamat.2005.11.001>.
- [43] Sandip Ghosh Chowdhury, Sudarsan Datta, B. Ravi Kumar, P.K. De, R.N. Ghosh, *Mater. Sci. Eng.* **2007**, *A 443*, 114, <https://doi.org/10.1016/j.msea.2006.09.059>.
- [44] B. Petit, N. Gey, M. Cherkaoui, B. Bolle, M. Humbert, *Int. J. Plast.* **2007**, *23*, 323, <https://doi.org/10.1016/j.ijplas.2006.07.002>.
- [45] H. Fujiwara, H. Inomoto, R. Sanada, K. Ameyama, *Scripta Materialia* **2001**, *44*, 2039, [https://doi.org/10.1016/S1359-6462\(01\)00858-2](https://doi.org/10.1016/S1359-6462(01)00858-2).
- [46] Takahiro KUSHIDA, *ISIJ International* **2003**, *43*, 470, <https://doi.org/10.2355/isijinternational.43.470>.
- [47] Eiji Akiyama, Katsuhiko Matsukado, Maoqiu Wang, Kaneaki Tsuzaki, *Corrosion Science* **2010**, *52*, 2758, <https://doi.org/10.1016/j.corsci.2009.11.046>.

In stainless steel (SS), the local austenite/ferrite distribution determines mechanical properties such as hardness and, close to the surface, affects the corrosion resistance. X-ray diffraction and near edge absorption analysis of bulk AISI 304 SS and thin films show that the concentration of ferrite, typically a typical minority phase in SS, strongly increases closer to the surface.

